Aerosol Jet Printing of a Benzocyclobutene-Based Ink as Adhesive Material for Wafer Bonding Application

Filippo Iervolino, Angelica Baldini, Ilaria Gelmi, Laura Castoldi, Raffaella Suriano,*
and Marinella Levi

Aerosol jet printing (AJP) is an emerging additive manufacturing technology that is gaining increasing attention in the electronic field. Several studies have been carried out on the AJP of conductive, semiconductive, and dielectric polymers for electronic applications. However, wafer bonding is an application that is still uncovered by literature. Therefore, in this work, the AJP of benzocyclobutene (BCB) as a polymeric adhesive for wafer bonding is presented for the first time. A thorough characterization of the processing parameters is carried out to identify the most ideal conditions for printing at a relatively high speed. Then, square patterns are printed, proving the versatility of the AJP technology in terms of the reachable thickness of the deposited BCB patterns. Complex patterns with a resolution of ≈60 µm are also printed. The bonding properties of the BCB are characterized from a morphological and mechanical point of view. In particular, the shear strength of the BCB coatings deposited with AJP is ≈39 MPa and it is comparable with the shear strength of BCB coating deposited by spin-coating. Consequently, AJP represents a valid alternative for the deposition of polymeric adhesive for wafer bonding.

1. Introduction

The need of the electronic industry for the production of components in a fast and cost-effective way is a demanding problem. Additive manufacturing (AM) represents a possible solution since it does not require the use of a mask and reduces at the minimum the material waste.[1–3] Among all the AM technologies, aerosol jet printing (AJP) is gaining increasing

interest due to its peculiar characteristics. The basic working principle of AJP consists of the generation of an aerosol from a functional ink, its transport toward the printing head, and the deposition onto a substrate.[4,5] Two types of aerosol jet printers exist based on the way the aerosol is generated: the ultrasonic and the pneumatic printer.[5] The ultrasonic printer uses a piezoelectric element to produce ultrasounds that generate the aerosol. The ultrasonic atomizer has the advantage of producing an aerosol with a low polydispersity and can print lines with a width down to 10 µm.[6–9] However, the ultrasonic printer can process inks with a maximum viscosity of 10 mPa s, which is a limiting factor for some types of inks.[5,6] The working principle of the pneumatic aerosol jet printer, instead, is represented in **Figure 1**a. A pneumatic aerosol printer consists of three main elements: an atomizer, a virtual impactor, and a printing head. A bubbler can also be present to prevent solvent evaporation during the printing process.[10,11] Figure 1b shows a schematic of the pneumatic atomizer. The ink enters the atomizing chamber due to the Venturi effect. The atomizer gas applies shear forces on the ink thus generating the aerosol droplets.[6,12] The atomizer gas has also the role to transport the aerosol toward the virtual impactor, represented in Figure 1c. In the virtual impactor, the excess atomizer gas and the smallest droplets of the aerosol (<1 µm) are removed by the application of an exhaust gas.[4,6] The high-density aerosol is then carried to the printing head, which is displayed in Figure 1d. In the printing head, there is the application of a third gas, called sheath gas, that has the twofold role of covering the nozzle wall and focusing the aerosol stream on the substrate.[13] The sheath gas is extremely important for the printing process since it prevents nozzle clogging allowing it to overcome issues present in other AM technologies, for example, inkjet printing, in which nozzle clogging occurs very frequently.[14] As opposed to the ultrasonic system, the polydispersity of the aerosol droplets is larger and the resolution that can be achieved is lower, being ≈50 µm.[5,15] However, a pneumatic atomizer allows the nebulization of inks with a viscosity of up to 1000 mPa s, which is fundamental when inks with high solid content need to be used.[13] Despite the several advantages of AJP, some issues are also present. It is a complex technology, which involves

F. Iervolino, R. Suriano, M. Levi
Department of Chemistry
Materials and Chemical Engineering "Giulio Natta"
Politecnico di Milano
Piazza Leonardo da Vinci 32, Milan, MI 20133, Italy
E-mail: raffaella.suriano@polimi.it
A. Baldini, I. Gelmi, L. Castoldi
STMicroelectronics
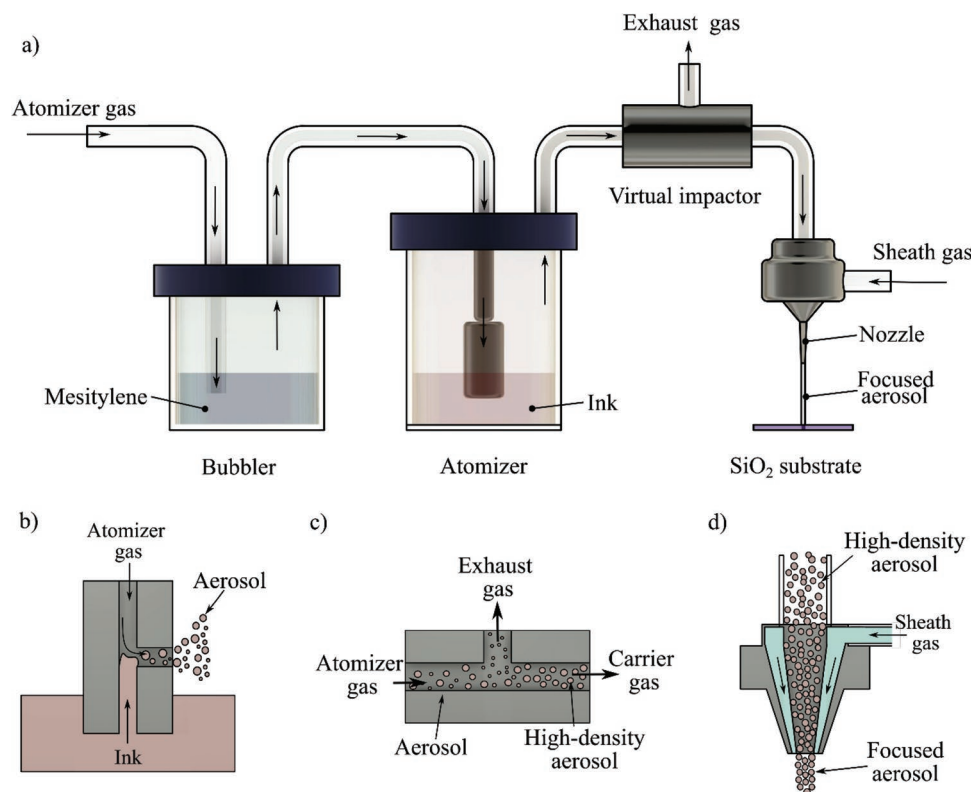Via Camillo Olivetti, 2, Agrate Brianza, MB 20864, Italy

Figure 1. a) Schematic representing the working principle of an aerosol jet printing head. Four main components are highlighted: the bubbler, the pneumatic atomizer, the virtual impactor, and the nozzle. b–d) Schematics representing the functioning of the pneumatic atomizer (b), the virtual impactor (c), and the nozzle (d).

many printing parameters. Indeed, several studies have been carried out on the effect of printing parameters on line width and thickness. However, it is important to highlight that the determination of the optimal parameters strongly depends on the type of ink, meaning that it is not feasible to predict the ideal parameters if a new material is used.[8,16,17] Literature agrees that using a lower atomizer gas flow rate (AtGFR), lower driving gas flow rate (DrGFR), that is, the difference between AtGFR and exhaust gas flow rate (ExGFR), higher sheath gas flow rate (ShGFR), and higher printing speed the line width is reduced. Whereas the effect on the line thickness is different, with a higher AtGFR, DrGFR, and ShGFR that produces an increase in the line thickness.[8,13,18–20]

However, overspray, one of the major defects that can happen in AJP, is much less understood.[18] Overspray is the deposition of small aerosol droplets in a non-focused area of the substrate. The phenomenon is due to the lower inertia of the small droplets that are not able to follow the aerosol stream and are pushed out of the focused area.[21,22] Some works in the literature studied the effect of the printing parameters on the overspray, focusing on ShGFR.[21–23] Nevertheless, Fuji-moto et al. stated that overspray is an intrinsic defect of the technology and that it strongly depends on the printed ink. Therefore, finding a correlation between printing parameters and overspray that works for all types of inks is still an unsolved problem.[18,24] AJP in the last decade has been studied for different types of applications, for example, biomedical, electrochemical, energy and electronics.[25–28] Considering

the electronic field, many types of inks have been studied (metallic, ceramic, and polymeric).[28,29] Among them, the most popular are inks loaded with silver nanoparticles, carbon nanotubes, and graphene.[30–32] The class of inks that is the least reported in the literature is the polymeric one. Some studies are present on some conductive, semiconductive, and dielectric polymeric inks.[33–46] Tarabella et al. and Hong et al. studied the effect of the focusing ratio (FR), that is, the ratio between the ShGFR and the DrGFR, on the line width and thickness of PEDOT:PSS lines to fabricate conductive patterns.[33,34] Zips et al., instead, used AJP printing to fabricate micro-needles made of PEDOT:PSS loaded with carbon nanotubes for bioelectronic applications.[35] Some works are present on the AJP polymers used as semiconductors, such as poly(3-hexylthiophene).[34,36–39] Other studies focused on the AJP of dielectric polymeric inks. Monne et al. synthesized aerosol jet printed polyvinyl alcohol aqueous solutions to fabricate sacrificial structures for micro-electromechanical systems (MEMS) production.[40] Wu et al. fabricated dielectric composite inks dispersing $Ca_2Nb_3O_{10}$ in a polymethylmethacrylate solution for thin-film transistors and characterized the dielectric properties of the material.[41] Ye et al., instead, aerosol jet printed an epoxy-based polymer as a passivation layer for electronic bio-sensing devices and characterized the processing parameters of the ink.[42] However, no works have been reported on the AJP of benzocyclobutene (BCB), which is a thermoset polymer widely used in the electronic industry for applications such as wafer bonding, interlayer dielectric, and 3D integration.[47–49]

**ADVANCED
SCIENCE NEWS**

www.advancedsciencenews.com

**ADVANCED
MATERIALS
INTERFACES**

www.advmatinterfaces.de

Furthermore, the works reported in the literature do not cover some applications of dielectric polymers, such as wafer bonding.

In this work, we present the AJP of BCB. First, the characterization of the ink properties and the effect of the printing parameters on lines are presented. Then squares and complex patterns were printed and characterized. Finally, wafer bonding was performed, and the adhesive properties of the material were evaluated.

2. Results and Discussion

2.1. Ink Characterization

The physical properties of the ink were characterized to qualitatively assess if the ink is printable with AJP. The viscosity was 52 mPa s and showed a Newtonian behavior in the tested shear rate range (Figure S1, Supporting Information). Therefore, we expected the material to be printable since its viscosity is below 1000 mPa s. Furthermore, the surface tension was 29.15 mN m^{-1} and the amount of solid material was 45 wt% measured by thermogravimetric analysis (Figure S2, Supporting Information). Also, this value is in the range considered printable by the literature, being the solid content below 75%.[6] We highlight that in a previous publication of ours we showed that this same ink was not printable with inkjet printing (IJP), meaning that AJP is a more versatile technique in terms of inks that can be printed.[50]

2.2. Printing Single Lines

2.2.1. Effect of Processing Parameters on the Line Width

To evaluate the resolution of the aerosol jet printer, an array of lines, that is, the smallest printable feature, was printed changing the process parameters. **Figure 2**a,b show the effect of the AtGFR on the line width keeping fixed the printing speed and the ShGFR, respectively. Increasing the AtGFR from 500 to 600 standard cubic centimeter per minute (SCCM) caused a slight increase in the line width, thus reducing the resolution. AtGFR is responsible for the increase in the line width since a higher AtGFR caused the nebulization of a higher quantity of ink for a second and consequently the deposited lines exhibited a higher width using a higher AtGFR. Figure 2a also exhibits that the effect of the AtGFR is strongly affected by the FR as well. At low FR, the increase in line width was much more evident than at higher FR. This is due to the focusing effect of higher FRs, which produces narrower lines, hindering the broadening effect caused by the increase in AtGFR. Moreover, an increase in printing speed produced a reduction in the line width. At higher printing speeds, the printing head spends less time on the substrate, allowing the deposition of a smaller amount of material. In other words, at higher printing speeds the material throughput on the substrate is lower. Figure 2c shows the effect of the DrGFR on the line width keeping fixed the AtGFR and the ShGFR and varying the printing speed. As expected, an increase in the line width with a higher DrGFR was observed.
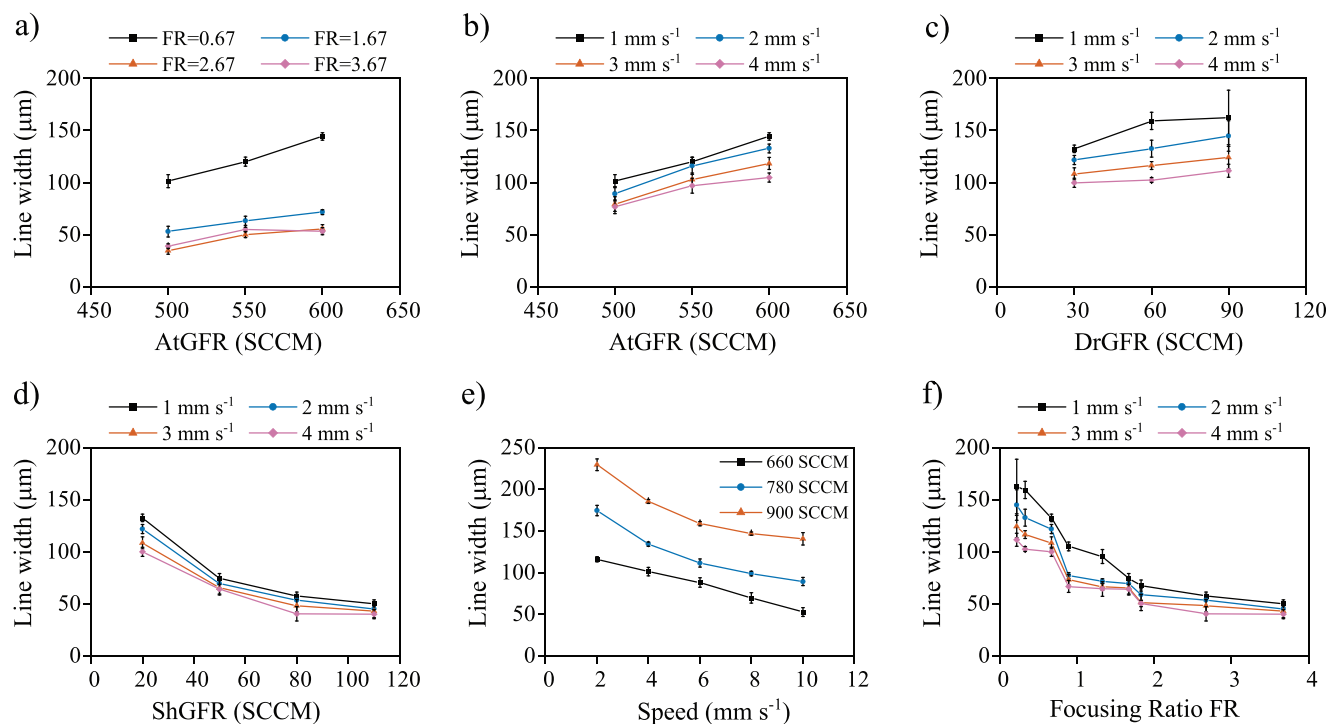

Figure 2. a) Effect of the AtGFR on the line width for different focusing ratios keeping fixed the ShGFR at 20 standard cubic centimeter per minute (SCCM) and the printing speed at 1 mm s^{-1}. b) Effect of the AtGFR on the line width for different printing speeds keeping fixed the DrGFR and the ShGFR at 30 and 20 SCCM, respectively. c) Effect of the DrGFR on the line width for different printing speeds keeping fixed the AtGFR and the ShGFR at 600 and 20 SCCM, respectively. d) Effect of the ShGFR on the line width for different printing speeds keeping fixed the AtGFR and the DrGFR at 600 and 30 SCCM, respectively. e) Effect of the printing speed varying the AtGFR and keeping fixed the DrGFR and the ShGFr at 30 and 20 SCCM, respectively. f) Effect of the FR on the line width varying the printing speed.

2202183 (3 of 11)

**ADVANCED
SCIENCE NEWS**

www.advancedsciencenews.com

**ADVANCED
MATERIALS
INTERFACES**

www.advmatinterfaces.de

Having a higher DrGFR means having a lower FR, which is responsible for a broader focus and thus a lower resolution. Furthermore, a high DrGFR is obtained by using a lower ExGFR. A lower ExGFR means that less material is removed at the virtual impactor, thus increasing the aerosol density, the material throughput, and consequently the line width. As in the case of the AtGFR, an increase in the printing speed caused a reduction in the line width. Figure 2d displays the effect of the ShGFR on the line width keeping fixed the AtGFR and the DrGFR. In this case, a different trend is observed. An increase in the ShGFR produced a reduction of the line width, since the FR is higher, thus increasing the resolution. A higher ShGFR causes a higher collimation of the aerosol stream. Therefore, the diameter of the aerosol stream ejected from the nozzle is lower, thus leading to a narrower line width on the substrate. It is also important to observe that the decrease in line width is much less pronounced when relatively high ShGFR values are used, that is, higher than 60 SCCM. Furthermore, the printing speed started to have a less pronounced effect from 40 SCCM and higher. Since for application in industries it is important to maximize the fabrication speed, the effect of printing at a relatively high speed was evaluated and the results are reported in Figure 2e. It was possible to reach a line width of $\approx$50 μm using an AtGFR of 660 SCCM. However, the line quality was poor, showing a not complete line coalescence. Consequently, the AtGFR was increased to 780 and 900 SCCM obtaining a line width of $\approx$100

and $\approx$150 μm, respectively. Therefore, printing at the maximum speed allowed by the machine (i.e., 10 mm s^{-1}) did not allow it to reach the minimum resolution maintaining a good printing quality. Figure 2f sums up the effect of the FR on the line width. For FR lower than 2 there is a sensible effect on the line width, while for FR higher than 2 the reduction in line width is slight, meaning that the focusing effect is lower. It is also important to notice that there is an enormous difference between printing at 1 mm s^{-1} and higher speed in terms of obtained line width until an FR of 2, then the difference is less pronounced. Instead, the difference between 2, 3, and 4 mm s^{-1} is evident until an FR of 1.

2.2.2. Effect of Processing Parameters on the Line Thickness

The effect of the processing parameters on the line thickness was evaluated as well to verify the versatility of the AJP technology in terms of the obtainable height of the coating. **Figure 3**a shows a comparison between the effect of the ShGFR on the line width and thickness. The observed trend for the line thickness is the opposite with respect to the line width. An increase in the ShGFR produced a decrease in the line width while the line thickness increased. The result agrees with the literature and is due to the focusing effect of the ShGFR that narrows the aerosol stream and deposits a higher quantity of material on a smaller section. The increase in thickness is
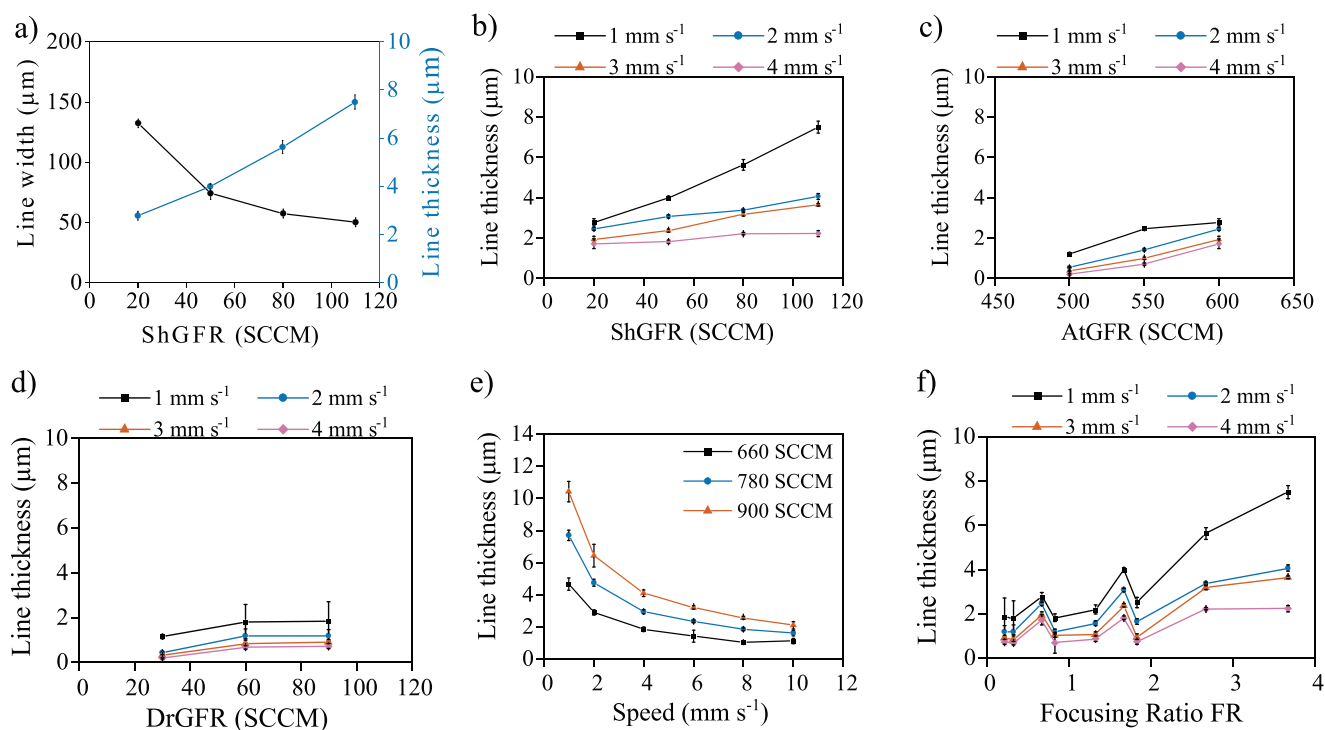

Figure 3. a) Effect of the ShGFR on the line width and thickness, keeping fixed the AtGFR, the DrGFR, and the printing speed at 600 SCCM, 30 SCCM, and 1 mm s^{-1}, respectively. b) Effect of the ShGFR on the line thickness for different printing speeds keeping fixed the AtGFR and the DrGFR at 600 and 30 SCCM, respectively. c) Effect of the DrGFR on the line width for different printing speeds keeping fixed the AtGFR and the ShGFR at 30 and 20 SCCM, respectively. d) Effect of the DrGFR on the line width for different printing speeds keeping fixed the AtGFR and the ShGFR at 500 and 20 SCCM, respectively. e) Effect of the printing speed varying the AtGFR and keeping fixed the DrGFR and the ShGFr at 30 and 20 SCCM, respectively. f) Effect of the FR on the line width varying the printing speed.

significant since it varied from ≈2 to ≈8 µm for an ShGFR of 20 and 110 SCCM, respectively. However, it is important to highlight that by increasing the ShGFR there is also a huge increase in the overspray, as shown in Figure S3, Supporting Information.

Figure 3b shows the effect of the increase in printing speed combined with the increase in ShGFR keeping fixed the AtGFR and the DrGFR. The increase in speed had an opposite trend with respect to the ShGFR, thus producing a decrease in the line thickness. The result can be explained by the fact that at a higher speed the aerosol stream spent less time on the same area, thus depositing less material. The effect of the DrGFR keeping fixed the AtGFR and the ShGFR is shown in Figure 3c. The DrGFR did not have a considerable influence on the line thickness, which showed just a slight increase in the thickness from 30 to 60 SCCM. Also, in this case, an increase in printing speed caused a reduction in the line thickness. Figure 3d displays the effect of the AtGFR on the line thickness keeping fixed the DrGFR and the ShGFR. An increase in the AtGFR produces an increase in the line thickness as well. The effect is more pronounced at higher AtGFRs, as shown in Figure 3e Indeed, it is possible to obtain a line thickness ranging from ≈1 to ≈10 µm changing the AtGFR from 500 to 900 SCCM. This is another proof of the versatility of the technology, which can print lines with a relatively large difference in thickness in just one pass. Figure 3e also shows the effect of printing with relatively high speed, in analogy to what was done in Section 2.2.1. Printing speeds had a huge influence on the line thickness since it decreased the value from ≈10 to ≈3 µm going from 1 to 10 mm s^{-1} in the case of an AtGFR of 900 SCCM. In the case of an AtGFR of 660 SCCM, the thickness values reached a plateau after 6 mm s^{-1}. The result is explained by the morphology of the line, which is not uniform and has some voids. At 900 SCCM, lines printed at all speeds exhibited a good morphology with no voids (Figure S4, Supporting Information). This is reflected by the fact that no plateau for the line thickness values was observed in the case of an AtGFR of 900 SCCM. Figure 3f shows the effect of the FR on the line thickness. In general, the line thickness tends to increase with increasing the FR. The effect is more pronounced for FR values higher than 2, while for values below 2 the line thickness is more stable.

2.3. Printing Square Patterns

Square patterns were printed to verify the effect of the printing parameters on a 2D geometry. We chose to use an ShGFR of 20 SCCM and a DrGFR of 30 SCCM since these were the values that produced the lines with the least amount of overspray. We varied the AtGFR and the printing speed to obtain squares with different thicknesses. **Figure 4**a shows a 1D profilometry of the printed squares printed at 1 mm s^{-1} and varying the AtGFR from 600 to 900 SCCM. The profile that is shown is referring to the center of squares and it is averaged for a width of 200 µm. The line width increased from 4 to 43 µm for AtGFRs of 600 and 900 SCCM, respectively. The huge increase in line width is due both to the higher amount of ink that it deposited and to the effect of the line coalescence, which is more pronounced for the square printed at 900 SCCM. Moreover, it is

possible to notice that all the squares exceeded the dimension of the design, that is, 1 mm × 1 mm. The broadening is due to the accumulation of material at the border of the print, and a higher quantity of material was deposited. Therefore, broadening should be considered when designing a pattern to avoid depositing the material in undesired locations. Figure S5, Supporting Information, shows that printing multiple layers is an alternative strategy to produce an increase in the thickness of the deposited coating. However, we consider this strategy not as interesting as changing the AtGFR since it increased the printing time and the overspray. Figure 4b shows the effect of the printing speed from 1 to 10 mm s^{-1} for squares printed with an AtGFR of 600 SCCM. The thickness of printed squares varies from 4 to less than 1 µm. Furthermore, the morphology of the printed squares started to worsen for a speed higher than 6 mm s^{-1}, showing irregularities and voids, meaning that the aerosol flow was not stable at a relatively high speed. Figure 4c displays the effect of the printing speed from 1 to 10 mm s^{-1} for squares printed with an AtGFR of 900 SCCM. For this flow rate, the thickness is decreased from 43 to 3.5 µm for printing speeds of 1 and 10 mm s^{-1}, respectively. The profilometry shows the gradual decrease of the thickness and the uniform morphology of the prints, meaning that the material deposition was stable at all used speeds. Figure 4d shows the microscopic images, the 2D and 3D representation of the optical profilometry for the square printed with an AtGFR of 900 SCCM at different printing speeds. At low printing speeds, the broadening phenomenon is very pronounced and there is also a loss of definition at the borders, especially at the corners of the squares. Instead, at printing speeds higher than 4 mm s^{-1}, the material started to accumulate on a preferential region of the print. The phenomenon was not expected and can be explained by the fact that the printing started from one side of the squares, producing a preferential drying direction. **Table 1** summarizes the thicknesses and the quality of the printed squares for all the tested parameters.

2.4. Printing Complex Patterns

Some complex patterns were printed to prove the feasibility of using AJP technology when small and complex geometries are present. **Figure 5** shows a printed interdigitated pattern, a serpentine pattern, and a bonding pattern, which was used in a previous publication of ours.[50] The AtGFR, DrGFR, ShGFR, and printing speed were 600 SCCM, 30 SCCM, 20 SCCM, and 1 mm s^{-1}, respectively. The interdigitated pattern was printed since it was characterized by small features, that is, 60 µm, that was close to the resolution limit of the machine for this ink. The serpentine pattern featured quite different shapes to test the AJP ability to fabricate different geometries. Finally, the bonding pattern was selected to evaluate the quality of the printer when cavities are present in a pattern. All the patterns were successfully printed, showing that AJP technology can be used when complex features are present. Moreover, the printed patterns could not be manufactured with conventional deposition technologies, such as spin-coating, thus proving one of the main advantages of AJP. The interdigitated pattern also showed the possibility of fabricating geometries close to
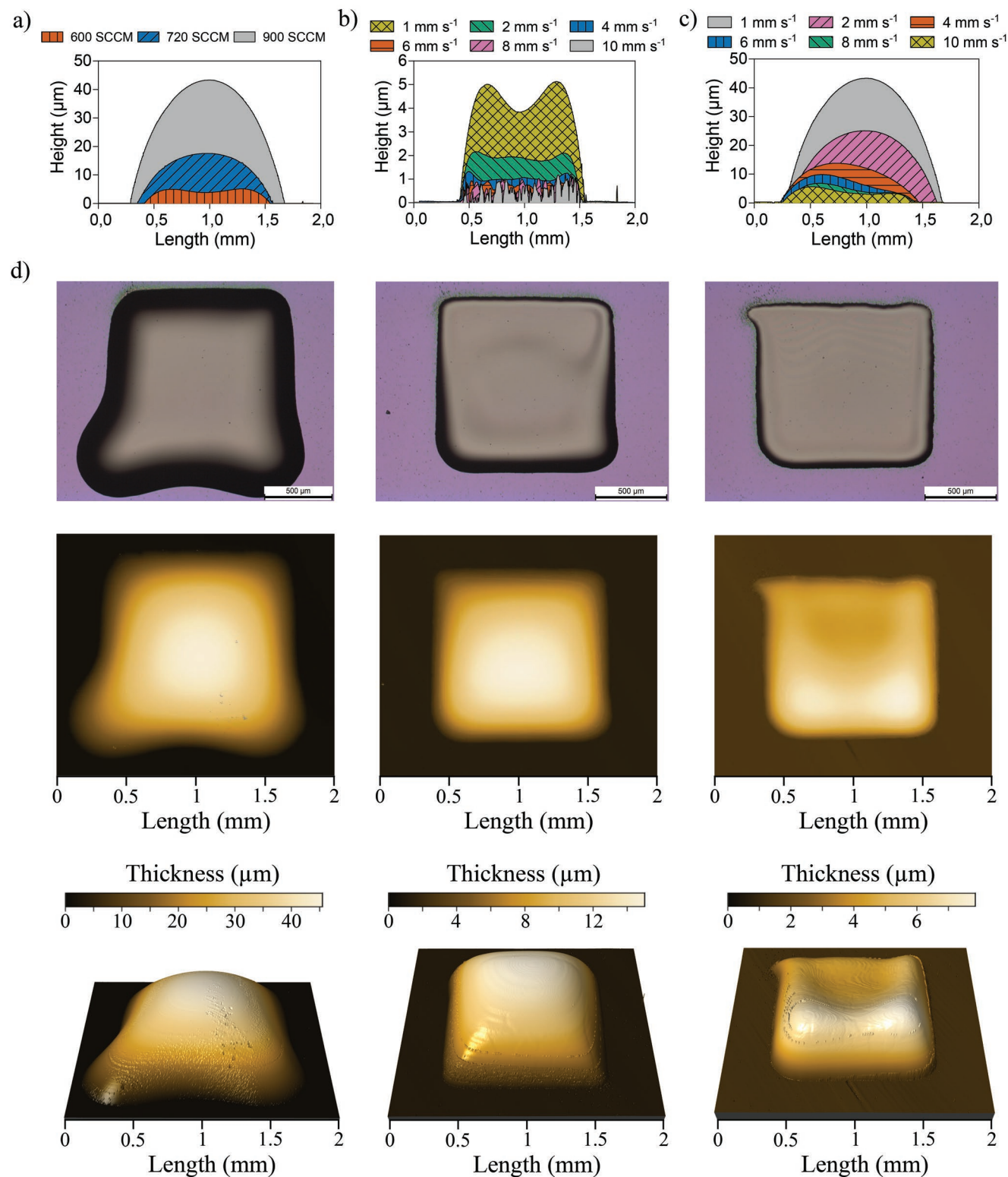
Figure 4. a) 1D profilometry of squares pattern printed at different AtGFR and keeping fixed the speed at 1 mm s⁻¹. b) 1D profilometry of squares pattern printed at different speeds keeping fixed the AtGFR at 600 SCCM. c) 1D profilometry of squares pattern printed at different speeds keeping fixed the AtGFR at 900 SCCM. d) Optical microscope image, 2D and 3D profilometry of squares pattern printed with an AtGFR of 900 SCCM and printing speeds of 1, 4, and 10 mm s⁻¹.

Table 1. Thickness values and qualitative evaluation of the quality of the squares printed at different AtGFRs and speeds keeping fixed the DrGFR and the ShGFR at 30 and 20 SCCM, respectively.

AtGFR [SCCM]	Speed [mm s^{-1}]	Thickness [µm]	Morphology of the print
600	1	4.03	Accumulation at the edges
	2	1.87	Accumulation at the edges
	4	0.98	Accumulation at the edges
	6	0.63	Incomplete coalescence
	8	0.48	Incomplete coalescence
	10	0.25	Incomplete coalescence
720	1	17.38	Uniform
	2	6.73	Uniform
	4	3.24	Uniform
	6	1.95	Uniform
	8	1.5	Uniform
	10	1.13	Accumulation on one side
900	1	43.12	Broadening
	2	24.81	Broadening
	4	13.62	Uniform
	6	7.58	Accumulation on one side
	8	5.21	Accumulation on one side
	10	3.29	Accumulation on one side

the resolution limit of the system, that is, 50 µm. The 60 µm width line was printed with no issues respecting the geometries imposed by the design. Overspray was present along the lines of the interdigitated patterns. However, the extension of the overspray was limited and did not completely cover the space between two adjacent lines. However, the serpentine pattern showed a much larger overspray. This is probably due to the larger lines of the serpentine pattern than the ones of the interdigitated pattern that required multiple passes, thus accumulating more over-sprayed particles. The bonding pattern proved the possibility of printing complex shapes featuring cavities with relatively low dimensions, that is, 225 µm × 200 µm for the cavities and 130 µm for the distance between two adjacent cavities. Also, in the case of this pattern, the geometry of the original design was respected. It is important to highlight that it was necessary to change the filling geometry from serpentine

to concentric to achieve good printing quality. Figure S6, Supporting Information, displays the difference between the two filling geometries, showing that the serpentine one produced elongated cavities that followed the printing direction. The difference in printing quality is based on the way the aerosol jet printer starts and interrupts the printing of a pattern. Since the atomization and the ejection of the aerosol stream cannot be stopped and restarted within seconds, a shutter is present to avoid the deposition of the aerosol stream on the substrate where it is not desired. In the case of the serpentine filler used for the bonding pattern (Figure S6b, Supporting Information), the shutter was activated several times when it approached the cavities since material deposition is not wanted inside the cavities. The sequential activation and deactivation of the cavities caused some instabilities in the material deposition and therefore a poor edge definition of the cavities. The concentric filling, instead, activated and deactivated the shutter just one time in correspondence with a cavity, thus leading to better printing quality. Overspray was still present, but it was limited to few tens of micrometers and did not completely obstruct the cavities.

2.5. Characterization of the Bonding Properties

2.5.1. Bonding Process

After characterizing the AJP process, we characterized the bonding quality of the material. Two Si wafers with a thermally grown oxide on the surface were bonded together using the bonding process reported in **Figure 6**a. The Si wafers were subjected to a first heating cycle at 150 °C for 30 min. This step allowed the BCB to flow and cover the surface of the wafers without leaving voids or inhomogeneity since the temperature is higher than its glass transition temperature (i.e., 23 °C) as shown in the differential scanning calorimetry (DSC) graph in Figure S7a, Supporting Information. Then, the temperature is set at 250 °C for 45 min. During this step, there was the crosslinking of the BCB generating the bonding of the Si wafers. Both these steps were performed while a piston was applying a force of 2.4 kN on the wafers. After the bonding, a gel content analysis was carried out to evaluate the amount of crosslinked material. The gel content was higher than 99%, proving the effectiveness of the bonding process toward the curing of BCB.
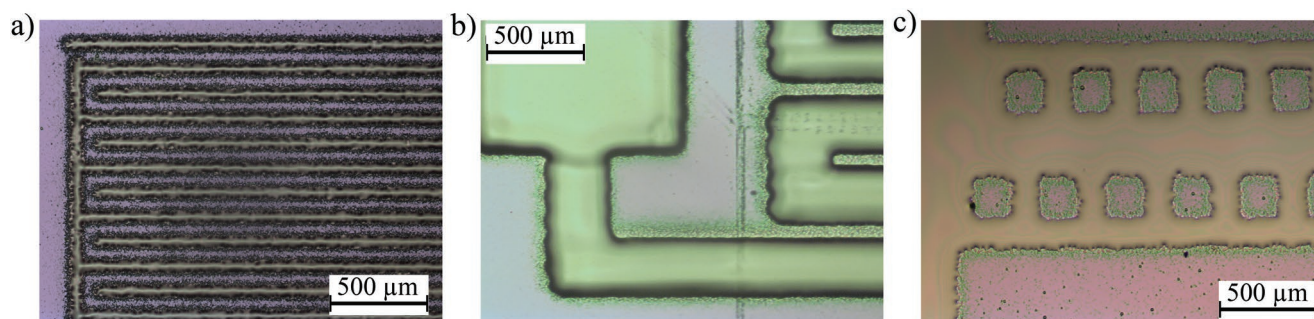

Figure 5. Optical microscope pictures of an a) interdigitated, b) serpentine, and c) bonding patterns printed with an AtGFR, a DrGFR, an ShGFR, and a printing speed of 600 SCCM, 30 SCCM, 20 SCCM, and 1 mm s^{-1}, respectively. The prints showed the feasibility of printing complex patterns with a resolution down to 60 µm, but with the presence of overspray.
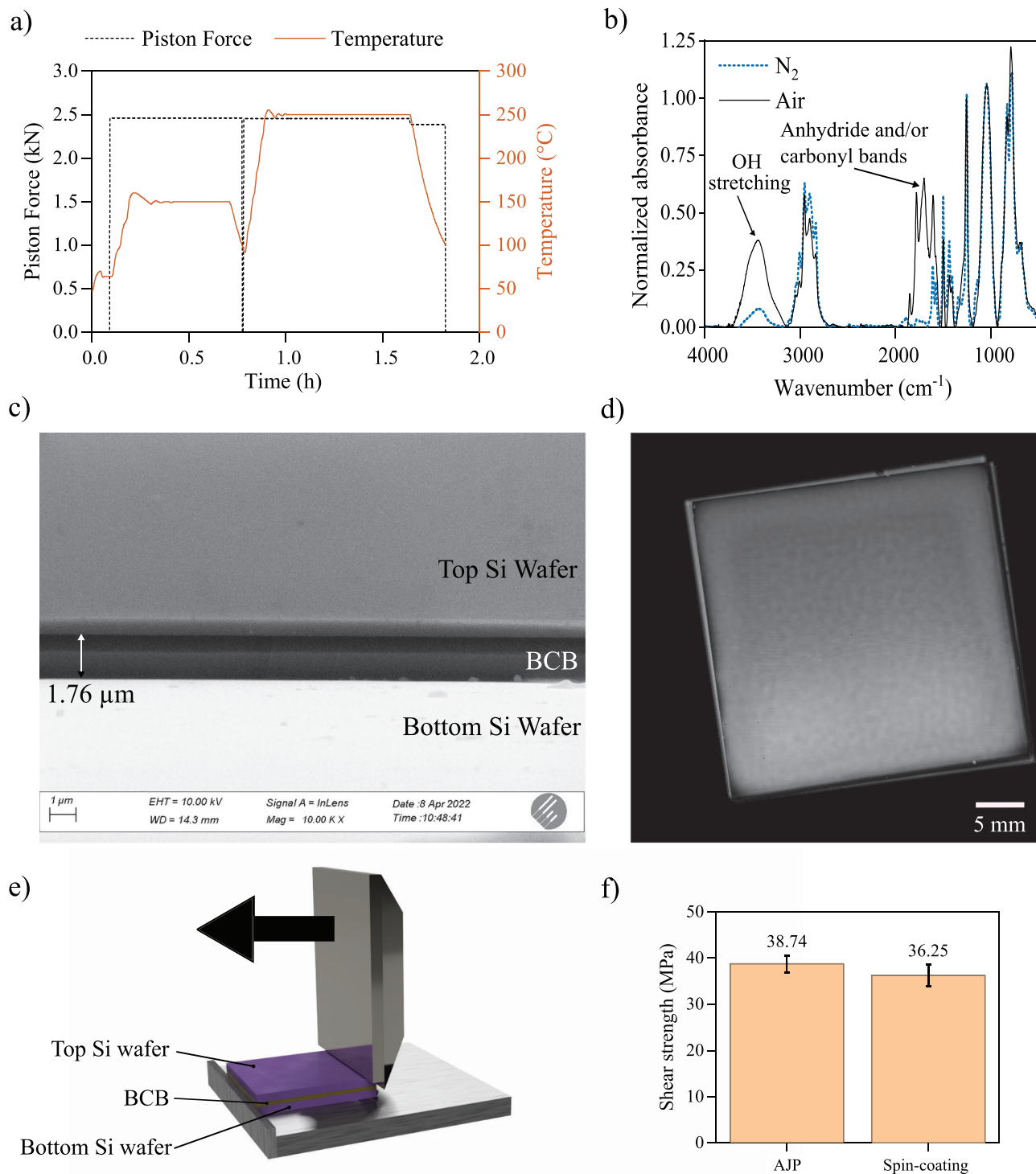
Figure 6. a) Graph showing the temperature and the force of the piston registered during the bonding step. b) FTIR spectra of the BCB subjected to the curing step in nitrogen and air atmosphere. c) Representative scanning electron microscopy (SEM) picture of the bonded Si wafers. d) Representative SAM of 3 cm × 3 cm bonded Si wafers. e) Schematic representing the die shear test performed on bonded Si wafers. f) Shear strength values obtained for bonded Si wafer using AJP and spin-coating to deposit BCB.

Moreover, BCB undergoes oxidation if the curing is carried out in an atmosphere containing oxygen. This phenomenon is reported by many works in the literature.[51–53] Furthermore, it was experimentally verified by oxidation induction time measurements reported in Figure S7b, Supporting Information, that as soon as oxygen was present during the curing step, oxidation

ADVANCED
SCIENCE NEWS
www.advancedsciencenews.com

ADVANCED
MATERIALS
INTERFACES
www.advmatinterfaces.de

of the material happened. To verify that during curing there was no oxidation, Fourier-transform infrared spectroscopy (FTIR) analysis was carried out. Figure 6b displays FTIR measurements on BCB cured in nitrogen and air atmosphere. The BCB cured in air showed a more intense peak at 3500–3200 cm^{-1} that is associated with the OH group stretching, meaning that there is a higher concentration of oxygen than the BCB cured in a nitrogen atmosphere. Moreover, the BCB cured in the air also showed the presence of anhydride and/or carbonyl bands at 1700–1850 cm^{-1}, which indicates the presence of oxidized benzylic CH$_2$ groups.[51]

2.5.2. Morphological Characterization of the Bonding

We evaluated the quality of the bonded wafers by scanning electron microscopy to observe if the BCB bonding layer was defect-free and homogeneous. The BCB ink was deposited on a 3 cm × 3 cm Si wafer using 780 SCCM, 30 SCCM, 20 SCCM, and 10 mm s^{-1} as AtGFR, DrGFR, ShGFR, and printing speed. Such parameters were selected to obtain a uniform coating with a thickness of ≈2 µm while minimizing the printing time. Figure 6c shows a representative scanning electron microscopy (SEM) image of the cross-section of the bonded Si wafers. The BCB coating is homogeneous and did not present any defects, meaning that both the deposition of the BCB on the bottom wafer and the bonding step were carried out successfully. The thickness of the coating was 1.76 µm, which is lower than the one measured for the deposited BCB before the bonding. The pressure applied during the bonding step slightly squeezes the BCB reducing the thickness of the bonding layer and helping to achieve a uniform coating over the whole Si wafers surfaces. Figure 6d displays a representative scanning acoustic microscopy (SAM) image of the bonded wafers. SAM also confirmed the good quality of the BCB deposition and the bonding since no defects were visible.

2.5.3. Die Shear Test

After the evaluation of the bonding quality, we performed die shear tests to assess quantitatively the shear strength of the material. The tests were performed on a pad having a constant cross-section for two reasons: i) to precisely calculate the shear strength and ii) to compare the coating deposited by AJP with the coating deposited using spin-coating. Shear tests carried out on complex patterns with a high aspect ratio would not have allowed a precise calculation of the shear strength and would not have been manufacturable with spin-coating, making the comparison impossible. Figure 6e shows a schematic of the die shear test. A tip applies a displacement on the top Si wafer while the bottom one is forced to not move due to the presence of a physical barrier. The test is successful when the bonding layer breaks and the force at which it happens is recorded.[54] Figure 6f displays the results of the die shear test for wafers bonded with a BCB layer deposited with AJP and spin-coating. Results showed a shear strength of 38.74 ± 1.88 and 36.25 ± 2.33 MPa for the BCB deposited with AJP and spin-coating, respectively. The values for the two depositions technique were comparable, meaning that the use of AJP did not negatively affect the bonding quality when compared to a

more traditional technology like spin-coating. Furthermore, our results are also comparable with values found in the literature for wafers bonded with BCB deposited using spin-coating.[55,56]

3. Conclusion

In this work, we proved for the first time the feasibility of depositing a BCB-based ink using AJP inks for wafer bonding applications. We thoroughly characterized the effect of the printing parameters to select the ideal processing parameter to print at a relatively high speed, that is, 10 mm s^{-1} while keeping a homogeneous line morphology. The printing of the squares pattern highlighted the versatility of the AJP technology since we obtained prints with a thickness ranging from 1 to 43 µm. The print of complex patterns also proved the possibilities of using AJP when complex geometries are present, such as interdigitated lines and cavities. Furthermore, we showed that complex geometries with features of ≈60 µm are printable. However, in all the prints, overspray was always present even though its extent was limited. The in-depth analysis of the printing parameters allowed us to identify the conditions that minimized the printing time while maintaining good print quality, allowing us to cover relatively large substrates (3 cm × 3 cm). The morphological characterization showed the good quality of the bonding process since no defects were visible. Moreover, the die shear test highlighted that the shear strength of BCB deposited with AJP is comparable with BCB deposited by spin-coating. Therefore, AJP represents a valid alternative to deposit polymeric adhesives such as BCB for wafer bonding applications. Future works might cover the development of quantitative models or estimates to predict the effect of the printing parameters and the comparison with the experimental results. Moreover, overspray is still an unsolved issue, and more efforts should be made to understand and avoid it. Furthermore, the AJP on patterned substrates with a high aspect ratio and their bonding could be proven.

4. Experimental Section

Materials: Cyclotene 3022–46 polymeric solution was purchased from Dow Chemicals. The polymeric solution consisted of a b-staged divinylsiloxane bisbenzocyclobutene dissolved in 1,3,5-trimethilbenzene, also known as mesitylene (MES).

Ink Characterization: The ink was characterized as reported in a previous publication.[50] Briefly, the rheological properties were characterized with a Kinexus Pro+ rotational rheometer (Malvern Panalytical) using a 40 mm cone-plate geometry. Surface tension was calculated by means of the pendant drop technique. The tests were performed using an OCA 20 (Data Physics), equipped with a 0.5 mL Hamilton glass syringe (Nglabtech) and a 1.65 mm diameter needle to dispense the material. A Q500 thermogravimetric analyzer (TA Instrument) was used to perform the thermo-gravimetric analysis (TGA) of the material. The tests were carried out in a nitrogen atmosphere from 25 to 800 °C with a heating rate of 20 °C min^{-1}. Dynamic and static DSC analyses were done with a DSC/832e provided by Mettler–Toledo. ≈15 mg of material were used for each test. The chosen scan rate for the dynamic analysis was 20 °C min^{-1}. A DSC3 (Mettler–Toledo) was used to perform static OIT analysis. Static analysis was performed following the ISO 11357–96:2018 standard. The analysis was performed at 250 °C since it is the curing temperature of BCB. The material was heated up at

2202183 (9 of 11)

**ADVANCED
SCIENCE NEWS**

www.advancedsciencenews.com

**ADVANCED
MATERIALS
INTERFACES**

www.advmatinterfaces.de

the selected temperature in a nitrogen atmosphere. Then, the air flow was activated, and it was kept for 60 min. FTIR analysis was performed with a Thermo Nicolet Nexus 670. Few µg of material were mixed with KBr powder. A tab was produced by means of a hydraulic press. The tab was then tested in transmission mode in air at room temperature in the range of 4000–500 cm^{-1}. For each measurement, 32 scans per test were performed at a resolution of 4 cm^{-1}. Gel content analyses were performed to evaluate the amount of crosslinked material after curing. ≈2 g of BCB were kept in toluene for 24 h under stirring. Then, the solution was filtered to collect non-solubilized particles. The solid residue was placed in a vacuum oven at 50 °C for 48 h to let the solvent evaporate. The gel percentage (Gel%), that is, the amount of crosslinked material, was computed using Equation (1):

$$\text{Gel}\% = \frac{m_{\text{solid}}}{m_{\text{sample}}} \cdot 100 \tag{1}$$

where m_{solid} is the mass of the solid residue and m_{sample} is the initial mass of the sample.

AJP: All the patterns were printed using a Ceradrop F4-Series (MGI group). The machine is equipped with an AJP system, schematically represented in Figure 1. The AJP is equipped with a bubbler containing MES, to limit solvent evaporation during nebulization. The atomizer is a pneumatic one, giving the possibility to nebulize inks with a viscosity of up to 1000 mPa s. For all the prints, a nozzle with a diameter of 200 µm was used and the nozzle-to-substrate distance was kept at 1 mm. The AtGFR war varied from 500 to 900 cm^3 min^{-1}, the DrGFR from 30 to 90 cm^3 min^{-1}, the ShGFR from 20 to 110 cm^3 min^{-1}, and the printing speed from 1 to 10 mm s^{-1}. Both the atomizer chamber and substrate were kept at 25 °C to avoid variability caused by the temperature. To guarantee stable printing performance, fresh inks were used at the beginning of each printing round to avoid negative effects caused by ink degradation and/or alteration. The ink showed stable printing performance up to 1 h of continuous printing. However, each printing round was stopped after 30 min to avoid any alteration. A thorough cleaning of all the components of the printer was performed. Furthermore, experiments were performed in different printing rounds to check the absence of variability between each printing round. The printer has two printing directions: the *x*-direction, meaning that the printing head is moving, and the *y*-direction, meaning that the substrate is moving. All the prints were carried out using the *x*-direction. All the patterns were printed on a Si substrate with a thermally grown oxide layer on top. Post-processing was performed on a hot plate at 150 °C for 15 min.

Patterns Characterization: A Leica INM 200 optical microscope was used to visualize the morphology of the prints. The microscope was in direct illumination mode and a 10× magnification objective was used. Metrology was performed by means of the software ImageJ. Profilm3D (Filmetrics) optical profilometer was employed to assess the thickness of the printed patterns. The profilometer was equipped with a Nikon DI objective with a 10× magnification. The measurements were performed using the white-light-interferometry mode, a pixel/area ratio of 1/4. Since both the substrate and the material are transparent to visible light, the application of a reflective coating was necessary to perform the measurements. Therefore, the samples were sputtered with gold before the profilometry tests.

Bonded Wafers Characterization: The bonding of the Si wafers was performed using a Gemini fully automated production wafer Evgbon wafer bonder. The process is done in vacuum to prevent oxidation of the BCB. The heating cycle consisted of two main steps: ramp to 150 °C and hold the temperature for 30 min followed by a ramp to 250 °C and hold the temperature for 45 min. The force applied by the piston was 2.4 kN. The morphology of the BCB bonding layer was evaluated by means of field emission SEM (Leo 1525, Zeiss). The samples were cleaved to obtain a brittle fracture to observe the cross-section. An acceleration voltage of 10 kV and a working distance of 14.3 mm were used. The quality of the bonding was qualitatively assessed by means of SAM (Sonix SAM Inspect). Die shear tests were carried out on two Si wafers bonded with BCB using a Nordson Dage 4000Plus.

Statistical Analysis: Unless otherwise specified, the reported values were obtained using the mean and the standard deviation computed on six measurements. Optical profilometry analysis was performed first leveling the data with the 3-point method and then averaging the thickness over a length of 200 µm.

Supporting Information

Supporting Information is available from the Wiley Online Library or from the author.

Acknowledgements

Conflict of Interest

The authors declare no conflict of interest.

Data Availability Statement

The data that support the findings of this study are available from the corresponding author upon reasonable request.

Keywords

[1] H. W. Tan, T. Tran, C. K. Chua, *Virtual Phys. Prototyping* **2016**, *11*, 271.

[2] J. Chang, X. Zhang, T. Ge, J. Zhou, *Org. Electron.* **2014**, *15*, 701.

[3] X. Zhang, T. Ge, J. S. Chang, *Org. Electron.* **2015**, *26*, 371.

[4] J. M. Hoey, A. Lutfurakhmanov, D. L. Schulz, I. S. Akhatov, *J. Nanotechnol.* **2012**, *2012*, 324380.

[5] J. Q. Feng, M. J. Renn, *J. Micro Nano-Manuf.* **2019**, *7*, 011004.

[6] N. J. Wilkinson, M. A. A. Smith, R. W. Kay, R. A. Harris, *Int. J. Adv. Manuf. Technol.* **2019**, *105*, 4599.

[7] Q. Huang, Y. Zhu, *Adv. Mater. Technol.* **2019**, *4*, 1800546.

[8] E. B. Secor, *Flexible Printed Electron.* **2018**, *3*, 035002.

[9] T. S. Srivatsan, T. S. Sudarshan, *Additive Manufacturing: Innovations, Advances, and Applications*, CRC Press, Boca Raton, FL **2015**.

[10] E. B. Secor, *Flexible Printed Electron.* **2018**, *3*, 035007.

[11] R. R. Tafoya, E. B. Secor, *Flexible Printed Electron.* **2020**, *5*, 035004.

[12] H. Abdolmaleki, P. Kidmose, S. Agarwala, *Adv. Mater.* **2021**, *33*, 2006792.

**ADVANCED
SCIENCE NEWS**

www.advancedsciencenews.com

**ADVANCED
MATERIALS
INTERFACES**

www.advmatinterfaces.de

[13] S. Binder, M. Glatthaar, E. Rädlein, *Aerosol Sci. Technol.* **2014**, *48*, 924.

[14] P. Viviani, E. Gibertini, F. Iervolino, M. Levi, L. Magagnin, *J. Manuf. Processes* **2021**, *72*, 411.

[15] K. R. May, *J. Aerosol Sci.* **1973**, *4*, 235.

[16] P. Kopola, B. Zimmermann, A. Filipovic, H.-F. Schleiermacher, J. Greulich, S. Rousu, J. Hast, R. Myllylä, U. Würfel, *Sol. Energy Mater. Sol. Cells* **2012**, *107*, 252.

[17] D. R. Hines, Y. Gu, A. A. Martin, P. Li, J. Fleischer, A. Clough-Paez, G. Stackhouse, A. Dasgupta, S. Das, *Addit. Manuf.* **2021**, *47*, 102325.

[18] A. Mahajan, C. D. Frisbie, L. F. Francis, *ACS Appl. Mater. Interfaces* **2013**, *5*, 4856.

[19] M. Smith, Y. S. Choi, C. Boughey, S. Kar-Narayan, *Flexible Printed Electron.* **2017**, *2*, 015004.

[20] E. Jabari, E. Toyserkani, *Carbon* **2015**, *91*, 321.

[21] G. Chen, Y. Gu, H. Tsang, D. R. Hines, S. Das, *Adv. Eng. Mater.* **2018**, *20*, 1701084.

[22] Y. Xiao, K. Kalaitzidou, D. Yao, W.-H. Yeo, T. A. L. Harris, *Adv. Mater. Interfaces* **2020**, *7*, 1902005.

[23] R. R. Salary, J. P. Lombardi, M. Samie Tootooni, R. Donovan, P. K. Rao, P. Borgesen, M. D. Poliks, *J. Manuf. Sci. Eng.* **2016**, *139*, 021015.

[24] K. T. Fujimoto, J. K. Watkins, T. Phero, D. Litteken, K. Tsai, T. Bingham, K. L. Ranganatha, B. C. Johnson, Z. Deng, B. Jaques, D. Estrada, *npj Flexible Electron.* **2020**, *4*, 32.

[25] N. X. Williams, N. Watson, D. Y. Joh, A. Chilkoti, A. D. Franklin, *Biofabrication* **2020**, *12*, 025004.

[26] L. J. Deiner, T. L. Reitz, *Adv. Eng. Mater.* **2017**, *19*, 1600878.

[27] J. K. Morzy, A. Sartor, W. M. Dose, C. Ou, S. Kar-Narayan, M. F. L. De Volder, C. Ducati, *Adv. Mater. Interfaces* **2022**, *9*, 2200530.

[28] K. B. Hon, L. Li, I. M. Hutchings, *CIRP Ann.* **2008**, *57*, 601.

[29] K.-S. Kwon, M. K. Rahman, T. H. Phung, S. Hoath, S. Jeong, J. S. Kim, *Flexible Printed Electron.* **2020**, *5*, 043003.

[30] A. K. Sinha, G. L. Goh, W. Y. Yeong, Y. Cai, *Adv. Mater. Interfaces* **2022**, *9*, 2200621.

[31] G. L. Goh, S. Agarwala, W. Y. Yeong, *Adv. Mater. Interfaces* **2019**, *6*, 1801318.

[32] E. Jabari, E. Toyserkani, *Mater. Lett.* **2016**, *174*, 40.

[33] G. Tarabella, D. Vurro, S. Lai, P. D'Angelo, L. Ascari, S. Iannotta, *Flexible Printed Electron.* **2020**, *5*, 014005.

[34] K. Hong, Y. H. Kim, S. H. Kim, W. Xie, W. D. Xu, C. H. Kim, C. D. Frisbie, *Adv. Mater.* **2014**, *26*, 7032.

[35] S. Zips, L. Grob, P. Rinklin, K. Terkan, N. Y. Adly, L. J. K. Weiß, D. Mayer, B. Wolfrum, *ACS Appl. Mater. Interfaces* **2019**, *11*, 32778.

[36] S. H. Kim, K. Hong, K. H. Lee, C. D. Frisbie, *ACS Appl. Mater. Interfaces* **2013**, *5*, 6580.

[37] Y. Xia, W. Zhang, M. Ha, J. H. Cho, M. J. Renn, C. H. Kim, C. D. Frisbie, *Adv. Funct. Mater.* **2010**, *20*, 587.

[38] M. Ha, W. Zhang, D. Braga, M. J. Renn, C. H. Kim, C. D. Frisbie, *ACS Appl. Mater. Interfaces* **2013**, *5*, 13198.

[39] C. Yang, E. Zhou, S. Miyanishi, K. Hashimoto, K. Tajima, *ACS Appl. Mater. Interfaces* **2011**, *3*, 4053.

[40] M. A. Monne, C. Q. Howlader, B. Mishra, M. Y. Chen, *Micromachines* **2021**, *12*, 220.

[41] X. Wu, F. Fei, Z. Chen, W. Su, Z. Cui, *Compos. Sci. Technol.* **2014**, *94*, 117.

[42] S. Ye, N. X. Williams, A. D. Franklin, *J. Electron. Mater.* **2022**, *51*, 1583.

[43] J. G. Tait, E. Witkowska, M. Hirade, T.-H. Ke, P. E. Malinowski, S. Steudel, C. Adachi, P. Heremans, *Org. Electron.* **2015**, *22*, 40.

[44] R. Eckstein, T. Rödlmeier, T. Glaser, S. Valouch, R. Mauer, U. Lemmer, G. Hernandez-Sosa, *Adv. Electron. Mater.* **2015**, *1*, 1500101.

[45] F. Zare Bidoky, C. D. Frisbie, *ACS Appl. Mater. Interfaces* **2016**, *8*, 27012.

[46] R. Eckstein, N. Strobel, T. Rödlmeier, K. Glaser, U. Lemmer, G. Hernandez-Sosa, *Adv. Opt. Mater.* **2018**, *6*, 1701108.

[47] S. Keyvaninia, M. Muneeb, S. Stanković, P. J. V. Veldhoven, D. V. Thourhout, G. Roelkens, *Opt. Mater. Express* **2013**, *3*, 35.

[48] M. E. Mills, P. Townsend, D. Castillo, S. Martin, A. Achen, *Microelectron. Eng.* **1997**, *33*, 327.

[49] N. W. Kim, H. Choe, M. A. Shah, D.-G. Lee, S. Hur, *Polymers* **2021**, *13*, 3633.

[50] F. Iervolino, R. Suriano, M. Scolari, I. Gelmi, L. Castoldi, M. Levi, *ACS Omega* **2021**, *6*, 15892.

[51] D. Burdeaux, P. Townsend, J. Carr, P. Garrou, *J. Environ. Monit.* **1990**, *19*, 1357.

[52] K. W. Paik, H. S. Cole, R. J. Saia, J. J. Chera, *J. Adhes. Sci. Technol.* **1993**, *7*, 403.

[53] Y. Kwon, J. Seok, J.-Q. Lu, T. S. Cale, R. J. Gutmann, *J. Electrochem. Soc.* **2005**, *152*, G286.

[54] D. Degryse, B. Vandevelde, E. Beyne, J. Degrieck, *J. Electron. Packag.* **2009**, *131*, 041003.

[55] A. Jourdain, P. D. Moor, K. Baert, I. D. Wolf, H. A. C. Tilmans, *J. Micromech. Microeng.* **2005**, *15*, S89.

[56] K.-I. Kim, J.-M. Kim, J.-M. Kim, G.-C. Hwang, C.-W. Baek, Y.-K. Kim, *J. Micromech. Microeng.* **2005**, *16*, 150.

2202183 (11 of 11)